Orbit design of a swarm for ultra-long wavelength radio interferometry with preliminary swarm and thruster sizing

Nevinskaia, Alisa S.; Bentum, Mark J.; Engelen, Steven; Monna, Bert; Naeije, Marc C.

DOI
10.1016/j.actaastro.2021.07.035

Publication date
2021

Document Version
Final published version

Published in
Acta Astronautica

Citation (APA)
Nevinskaia, A. S., Bentum, M. J., Engelen, S., Monna, B., & Naeije, M. C. (2021). Orbit design of a swarm for ultra-long wavelength radio interferometry with preliminary swarm and thruster sizing. *Acta Astronautica*, *188*, 463-472. https://doi.org/10.1016/j.actaastro.2021.07.035

Acta Astronautica 188 (2021) 463–472

Contents lists available at ScienceDirect

Acta Astronautica

journal homepage: www.elsevier.com/locate/actaastro

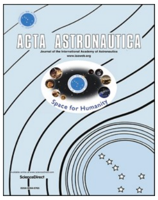

Orbit design of a swarm for ultra-long wavelength radio interferometry with preliminary swarm and thruster sizing

Alisa S. Nevinskaia [a,b,*], Mark J. Bentum [c,d], Steven Engelen [b], Bert Monna [b], Marc C. Naeije [a,**]

[a] Delft University of Technology, Faculty of Aerospace Engineering, Kluyverweg 1, 2629 HS, Delft, the Netherlands
[b] Hyperion Technologies, Vlinderweg 2, 2623 AX, Delft, the Netherlands
[c] Eindhoven University of Technology, Faculty of Electrical Engineering, Groene Loper 3, 5612 AE, Eindhoven, the Netherlands
[d] ASTRON, Netherlands Institute for Radio Astronomy, Oude Hoogeveensedijk 4, 7991 PD, Dwingeloo, the Netherlands

ARTICLE INFO

Keywords:
Ultra-long wavelength radio interferometry
Radio astronomy
Orbit design and optimisation
Heliocentric Earth leading orbit
Distributed satellite swarms
Swarm and thruster sizing

ABSTRACT

Observing the universe in the Ultra-Long Wavelength (ULW) regime has been called the 'last frontier in astronomy'—real imaging capabilities here are yet to be achieved. Obtaining an image of the sky in this frequency band can be done by employing a swarm of satellites that together act as an interferometer and collect the required imaging information pieces throughout the course of their operational life. Meeting the mission objective is challenging for such a swarm, since this imposes restrictions on the operational environment and the relative position and velocity vectors between the swarm elements. This work proposes an orbit solution in a Heliocentric Earth-Leading Orbit (HELO) for an autonomous CubeSat swarm with chemical thrusters. A distributed formation flying algorithm is used to aid the collection of the required imaging information pieces. Furthermore, the estimated total mission launch mass is reduced by optimising cost functions and finding favourable position and velocity at start of operational life, as well as by finding favourable thrust manoeuvre patterns. The results show that the mission objective—obtaining a 3D map of the Universe in ULW—can be achieved with 68 6U spacecraft (S/C). Moreover, the swarm can remain in a Radio Frequency Interference (RFI) quiet zone of $>5 \times 10^6$ km, whilst not drifting further than $\sim 6.6 \times 10^6$ km from Earth for an operational life of one year.

1. Introduction

Although the idea of space-based radio astronomy, to overcome ionospheric effects, dates back to when space exploration was still in its infancy [17–19,28], real imaging capabilities in the ULW regime (0.1–30 MHz) are—in contrast to all other major wave bands—currently yet to be achieved. Imaging in this virtually unexplored region is driven by a multitude of science cases (e.g. seeking the Dark Ages signal—an echo of the era from before the first stars were born) and could impact our knowledge of the Universe in an unprecedented way [7,13,23,33,46].

Acquiring real imaging capabilities in the ULW regime is challenging, because it demands that a stringent set of requirements regarding the instrument's operational environment, span and dynamic behaviour is met. To start with, the instrument must operate in an environment where the background noise levels (RFI) are sufficiently low with respect to the signals of interest (Cosmic Radio Background (CRB)). More specifically, the assumption can be made that the CRB signal should be ~ 3 dB above RFI [5,33]. Since Earth is a major source of RFI (which has both man-made as well as natural causes, such as lightning, see e.g. Ref. [23]), Earth orbits are not suitable and an operational location in deep space must be selected—either at the far side of the Moon (as has previously been shown by the Radio Astronomy Explorer 2 (RAE-2) mission, see Ref. [1]) or $\sim 5 \times 10^6$ km from Earth [5,33] (Bentum and Boonstra [5] conclude this based on extrapolations of RFI measurements from a number of previous missions). Next to that, to achieve the required angular resolution, the instrument must have a span of up to $\sim$ 100 km. Angular resolution $_1$ is the ratio between the wavelength λ and the aperture D of a monolithic telescope or the maximum baseline length $\|s_{ij}\|_{max}$ of an interferometer: $\alpha \approx \lambda / D \approx \lambda / \|s_{ij}\|_{max}$ [33]; note here that an interferometer is a distributed telescope that comprises multiple smaller antennas; an

---

[*] Corresponding author. Delft University of Technology, Faculty of Aerospace Engineering, Kluyverweg 1, 2629 HS, Delft, the Netherlands.
[**] Corresponding author.

E-mail addresses: a.nevinskaia@hyperiontechnologies.nl (A.S. Nevinskaia), M.C.Naeije@tudelft.nl (M.C. Naeije).

https://doi.org/10.1016/j.actaastro.2021.07.035
Received 3 November 2020; Received in revised form 10 June 2021; Accepted 22 July 2021

interferometer baseline s_{ij} is the relative position vector between each two of its antennas; a baseline length $\left\|s_{ij}\right\|$ is the magnitude of s_{ij}. Theoretically, the maximum attainable α for frequencies below 30 MHz is limited to ~ 1 arcminute (this is due to a number of physical phenomena, such as wave propagation in the Interstellar Medium (ISM) and the Interplanetary Medium (IPM), see e.g. Ref. [30]). To reach this resolution, the instrument must have a span (D or $\left\|s_{ij}\right\|_{max}$) of ~ 100 km [15,33]. Since making a monolithic telescope of ~ 100 km in aperture is physically not achievable, the ULW instrument must be an interferometer. However, collecting Imaging Information Pieces.

(IIPs) with an interferometer imposes restrictions on the relative dynamic behaviour of its antennas; because, whilst a monolithic telescope collects all IIPs, that are needed to form one image, simultaneously using one single rigid antenna, an interferometer collects the different IIPs over time (by changing its antenna configuration w.r.t. the imaging target), using at least two antennas that can potentially move w.r.t. one another. These different IIPs can eventually be put together and processed to form a synthesised image. The objective of a ULW instrument is to ideally enable a 3D map of the full sky (capture all signals in all directions), in which the signals are visualised clearly (are e.g. not smeared); the quality of the synthesised image can thus be classified by its level of coverage and clarity, respectively. Logically, the quality of the synthesised image depends on the characteristics of the IIPs from which it is synthesised. Notably, the characteristics of each IIP depend on the characteristics of the baseline state $S_{ij} = [s_{ij}, \dot{s}_{ij}]^T$ at which it was obtained. Therefore, the quality of the synthesised image can be determined by analysing whether a collection of baseline states $\mathbb{B} = \left\{\mathbb{b}, \dot{\mathbb{b}}\right\}^T = \left\{\left\{s_{ij}^1, s_{ij}^2, \ldots, s_{ij}^q\right\}, \left\{\dot{s}_{ij}^1, \dot{s}_{ij}^2, \ldots, \dot{s}_{ij}^q\right\}\right\}^T$, that is subject to a number of requirements, has been achieved by the interferometer throughout its operational life. Note here that the orientation of s_{ij} determines in what direction the sky is mapped, whilst its length $\left\|s_{ij}\right\|$ determines the size of the background structure that is mapped (longer baseline lengths can capture smaller background structures, whereas shorter baseline lengths can capture larger ones); $\left\|\dot{s}_{ij}\right\|$ is of influence on the clarity of each IIP (because the CRB signals are weak, an increase in exposure time is required, during which $\left\|\dot{s}_{ij}\right\|$ must remain sufficiently low to prevent smearing of signals). For a more in depth explanation on how and why the quality of a synthesised image can be derived from the achieved baseline states, the interested reader can consult e.g. Refs. [10,38]; furthermore, for a derivation of the requirements on $\mathbb{B}$, the interested reader can consult e.g. Refs. [15,23,33]. This work includes only an overview of these $\mathbb{B}$ -requirements, as they have previously and extensively been covered by others. In short, the dynamic behaviour of the antennas (i.e. interferometer elements or S/C) should: enforce a large collection of unique baselines $\mathbb{b} = \left\{s_{ij}^1, s_{ij}^2, \ldots, s_{ij}^q\right\}$, where $s_{ij}^1 \neq s_{ij}^2 \neq \ldots \neq s_{ij}^q$ and q is the total number of baselines $\in \mathbb{b}$ (q is thus the size of $\mathbb{b}$); whilst keeping $\left\|s_{ij}\right\| \leq 100$ km $\forall s_{ij} \in \mathbb{b}$; and whilst keeping the baseline speed $\left\|\dot{s}_{ij}\right\| \leq 3 \ \mathrm{m/s} \ \forall \dot{s}_{ij} \in \dot{\mathbb{b}}$, where $\dot{\mathbb{b}} = \left\{\dot{s}_{ij}^1, \dot{s}_{ij}^2, \ldots, \dot{s}_{ij}^q\right\}$ holds the set of baseline velocity vectors $\dot{s}_{ij}$ that correspond to their respective $s_{ij} \in \mathbb{b}$. Then, the level of coverage $Q_{\%}$ is defined by q: $Q_{\%} = q/\ Q_{max} \times\ 100\%$; here, Q_{max} is a design parameter. The specification and requirements regarding $Q_{\%}$, Q_{max} and q, shall in this work be defined analogously to the work of Dekens et al. [15]: real imaging capabilities of the full sky require that $Q_{\%} \geq 95\%$, which with a voxel size of 1 km^3 (i.e., all $s_{ij} \in \mathbb{b}$ are rounded off to whole km), gives $Q_{max} \sim 4.2 \times 10^6$, and amounts to $q \geq\sim 4.0 \times 10^6$. For a further explanation on and a derivation of $Q_{\%}$ and Q_{max}, the interested reader can consult Dekens et al. (in short, Q_{max} can be derived from the span of the instrument in 3D and its voxel resolution—more specifically, it is the number of voxels (3D pixels or cubes) of 1 km^3, that fit into a theoretical sphere of 100 km in radius).

Currently, space-based imaging in the ULW-band remains still in the monolithic domain, with aperture sizes reaching the order of meters at best (see e.g. the Cassini [29] and the Stereo [24] missions)—rendering real imaging capabilities far from achieved. Previously, several conceptual studies have been proposed. Among others [2,12,14,25] have suggested lunar surface arrays at the far-side of the Moon. The effects on imaging capabilities of electrostatic properties of lunar dust and lunar ionosphere would have to be considered in the design of such arrays [12,36] (note that the imaging capabilities can be affected by the presence of free electrons and other charged particles, which can scatter and distort radio-waves). Burns et al. [11] propose a study of the Dark Ages signal in the 40–120 MHz band in low selenocentric orbits and mention that a number of processes that can impact imaging capabilities produce most of its emission at frequencies below 40 MHz—rendering lunar-based and low lunar orbits less suitable for imaging at ≤ 30 MHz. Others have proposed studies for orbiting arrays (in a variety of orbits), such as Low Frequency Space Array (LFSA) [47], Formation-flying sub-Ionospheric Radio astronomy Science and Technology (FIRST) [8], Distributed aperture Array for Radio astronomy In Space (DARIS) [9] and Orbiting Low Frequency Antennas for Radio Astronomy (OLFAR) [6]—some of which suggest the use of readily available off the shelf technology to reduce mission cost or a distributed communication architecture to make the swarm robust to single point failures. However, none of these studies have explicitly shown compliance with the collection of aforementioned requirements. Moreover, despite the highly promising scientific return potential of ULW swarms, few in-depth orbit design studies have been performed [7,33]. Orbitographic design and analysis is necessary to define the extent in which the IBrequirements are met; and, to estimate the swarm size required to this end. Dekens et al. [15] performed an orbitographic study for the OLFAR concept in lunar orbits and concluded that a coverage of ~ 77 % was feasible with ~ 100 S/C, after optimisation of the initial state (initial conditions at orbit insertion). However, Dekens et al. [15] indicated that an important requirement could not be met in lunar orbits: the baseline speed $\left\|\dot{s}_{ij}\right\|$ was a factor ~ 10 higher than required.

In this article, we propose an orbit solution that complies with the full set of aforementioned requirements. We use well known models and methods to this end. Our design involves a CubeSat swarm in a HELO, inserted at $\sim 5 \times 10^6$ km from Earth, with distributed communication and chemical thrusters for actuation. Actuation is used to decrease the number of S/C needed to reach $Q_{\%} \geq 95\%$ (thus to improve cost efficiency, by reducing the total mission mass) as well as for orbit maintenance (also to improve cost efficiency: by reducing the natural drift from Earth that occurs over time in HELO orbits, the required power for telemetry—and thus the mass of the power subsystem—can be reduced). Chemical thrusters are selected even though propulsion systems that are based on expulsion of charged particles (e.g. electric and ion systems) offer a higher power density [39] and could thus lead to a more mass (and thus potentially cost) efficient solutions. However, such systems are not suitable, because the expulsion of charged particles can scatter and distort radio waves and thus diminish imaging capabilities.

We must add that the presented solution encompasses a preliminary mission feasibility study and assumes ideal conditions: no failures; ideal performance; the aspect of collision avoidance is disregarded. The significance of these assumptions on the final design should be investigated in future research. However, note that the aforementioned previously proposed orbit design concepts, e.g. by Dekens et al. [15], have not included these aspects in their simulations either (the Technology Readiness Level (TRL) for a space-based interferometer with a distributed communication architecture is simply still quite low).

This paper is organised in the following manner: in Section 2, the mission objective with its set of requirements is summarised; in Section 3, the equations of motion are defined; in Section 4, a number of hardware parameters are defined; in Section 5, cost functions are defined that aid in the reduction of total swarm mass and the results are discussed; in Section 6 the discussion and in Section 7 the conclusion is provided.

2. Problem definition

The problem regarding the $\mathbb{B}$ -requirements can be defined more specifically in terms of the following system. Consider an interferometer comprising N S/C that are defined by the set $\mathscr{N} = \{1, 2, \ldots, N\}$ and with S/C elements i and j for which holds: $i, j \in \{\mathscr{N} | i \neq j\}$ (i.e., elements i and j can be any two distinct S/C in the S/C swarm). The state $\boldsymbol{S}_i = [\boldsymbol{s}_i,\ \dot{\boldsymbol{s}}_i]^T$ of element i at time t can be defined by the position vector $\boldsymbol{s}_i(t) = [x_i(t), y_i(t), z_i(t)]^T$ and the velocity vector $\dot{\boldsymbol{s}}_i(t) = [\dot{x}_i(t), \dot{y}_i(t), \dot{z}_i(t)]^T$ expressed in reference frame $\mathscr{F}_o(X_o, Y_o, Z_o)$ ($\boldsymbol{S}_j(t)$ is defined in an analogous way), where $\mathscr{F}_o$ is a right handed inertial reference frame (i.e., the centre of the reference frame is the system's barycentre and the frame is non-rotating w.r.t. the sky), in which the $\{X_o, Y_o\}$ -axes lie in the plane defined by the movement of Earth around the Sun and Z_o is normal to that plane. Then, the baseline $\boldsymbol{s}_{ij}$ and the baseline rate $\dot{\boldsymbol{s}}_{ij}$, formed at time t by i and j are:

$$\begin{aligned} \boldsymbol{s}_{ij}(t) &= \boldsymbol{s}_j(t) - \boldsymbol{s}_i(t) = \left[u_{ij}(t), v_{ij}(t), w_{ij}(t)\right]^T \\ \dot{\boldsymbol{s}}_{ij}(t) &= \dot{\boldsymbol{s}}_j(t) - \dot{\boldsymbol{s}}_i(t) = \left[\dot{u}_{ij}(t), \dot{v}_{ij}(t), \dot{w}_{ij}(t)\right]^T \end{aligned} \tag{1}$$

where $u_{ij}(t) = x_j(t) - x_i(t)$, $v_{ij}(t) = y_j(t) - y_i(t)$, $\dot{w}_{ij}(t) = \dot{z}_j(t) - \dot{z}_i(t)$, etc. The part of the notation that indicates the time will be omitted henceforward. The corresponding baseline length $\|\boldsymbol{s}_{ij}\|$ and baseline speed $\left\|\dot{\boldsymbol{s}}_{ij}\right\|$ are defined as:

$$\begin{aligned} \|\boldsymbol{s}_{ij}\| &= \sqrt{u_{ij}^2 + v_{ij}^2 + w_{ij}^2} \\ \left\|\dot{\boldsymbol{s}}_{ij}\right\| &= \sqrt{\dot{u}_{ij}^2 + \dot{v}_{ij}^2 + \dot{w}_{ij}^2} \end{aligned} \tag{2}$$

In this work, the mission's operational life is assumed to be 1 year (365.25 days). Then, the mission objective can be summarised in the following way (see also Section 1): the S/C swarm must have achieved the collection of baseline states $\mathbb{B}$, expressed in $\mathscr{F}_o$, that satisfies the imaging conditions (Eq. (3)(ad)) and can meet the imaging objective (Eq. (3)(e)), whilst complying with the mission requirement $T_{ops} =$ 1 year (Eq. (3)(*f*)):

$$\mathbb{B} = \left\{ \begin{array}{c} [\mathbb{b}]^{\text{km}} \\ \dot{\mathbb{b}} \end{array} \right\} = \left\{ \begin{array}{cccc} \left[\boldsymbol{s}_{ij}^1\right]^{\text{km}}, & \left[\boldsymbol{s}_{ij}^2\right]^{\text{km}}, & \ldots, & \left[\boldsymbol{s}_{ij}^q\right]^{\text{km}} \\ \dot{\boldsymbol{s}}_{ij}^1, & \dot{\boldsymbol{s}}_{ij}^2, & \ldots, & \dot{\boldsymbol{s}}_{ij}^q \end{array} \right\} \tag{3}$$

$$\begin{cases} \|\boldsymbol{s}_{ij}\| \leq 100\ \text{km}, \forall \boldsymbol{s}_{ij} \in \mathbb{b} & \text{(a)} \\ \left\|\dot{\boldsymbol{s}}_{ij}\right\| \leq 3\ \text{m}/\text{s}, \forall \dot{\boldsymbol{s}}_{ij} \in \dot{\mathbb{b}} & \text{(b)} \\ \left[\boldsymbol{s}_{ij}^1\right]^{\text{km}} \neq \left[\boldsymbol{s}_{ij}^2\right]^{\text{km}} \neq \ldots \neq \left[\boldsymbol{s}_{ij}^q\right]^{\text{km}} & \text{(c)} \\ \|\boldsymbol{s}_{\oplus i}\| \geq 5 \times 10^6\ \text{km} & \text{(d)} \\ q \geq\sim 4.0 \times 10^6 & \text{(e)} \\ T_{ops} = 365.25\ \text{days} & (f) \end{cases}$$

Here, the notation $[\boldsymbol{s}_{ij}]^{\text{km}}$ denotes that all components of $\boldsymbol{s}_{ij}$ are rounded off to the nearest integer in km; $\|\boldsymbol{s}_{\oplus i}\| = \sqrt{(x_i - x_\oplus)^2 + (y_i - y_\oplus)^2 + (z_i - z_\oplus)^2}$ is the distance between i and the centre of mass of Earth $\boldsymbol{s}_\oplus = [x_\oplus, y_\oplus, z_\oplus]^T$.

3. Equations of motion

A set of S/C $\mathscr{N}$, will have achieved throughout its T_{ops}, a collection of states $\mathbb{S}_{\mathscr{N}}$ (the swarm ephemeris):

$$\mathbb{S}_{\mathscr{N}} = \begin{bmatrix} \boldsymbol{S}_1(t_0) & \boldsymbol{S}_1(t_0 + \Delta t) & \cdots & \boldsymbol{S}_1(t_{end}) \\ \boldsymbol{S}_2(t_0) & \boldsymbol{S}_2(t_0 + \Delta t) & \cdots & \boldsymbol{S}_2(t_{end}) \\ \vdots & \vdots & \ddots & \vdots \\ \boldsymbol{S}_N(t_0) & \boldsymbol{S}_N(t_0 + \Delta t) & \cdots & \boldsymbol{S}_N(t_{end}) \end{bmatrix} \tag{4}$$

Here, t_0 and t_{end} denote the time at the beginning and at the end of operational life, respectively; Δt is the time interval on which the ephemeris is stored. Note that $\mathbb{B}$ (Eq. (3)) can be fully defined from $\mathbb{S}_{\mathscr{N}}$ (Eq. (4)). Then, $\mathbb{S}_{\mathscr{N}}(t_0 + \Delta t)$ can be obtained by integrating the dynamics $\dot{\boldsymbol{S}}_i(t) = \left[\dot{\boldsymbol{s}}_i(t), \ddot{\boldsymbol{s}}_i(t)\right]^T = \left[\dot{x}_i(t), \dot{y}_i(t), \dot{z}_i(t), \ddot{x}_i(t), \ddot{y}_i(t), \ddot{z}_i(t)\right]^T$ over a time interval Δt, to obtain $\boldsymbol{S}_i(t + \Delta t) = \left[\boldsymbol{s}_i(t + \Delta t), \dot{\boldsymbol{s}}_i(t + \Delta t)\right]^T = [x_i(t + \Delta t), y_i(t + \Delta t), z_i(t + \Delta t), \dot{x}_i(t + \Delta t), \dot{y}_i(t + \Delta t), \dot{z}_i(t + \Delta t)]^T$, $\forall i \in \mathscr{N}$; $\dot{\boldsymbol{S}}_i(t)$ is defined by the external and the internal dynamics models, f_{ex} and f_{in}, respectively:

$$\dot{\boldsymbol{S}}_i = \underbrace{\dot{\boldsymbol{S}}_i|_{ex}}_{f_{ex}} + \underbrace{\dot{\boldsymbol{S}}_i|_{in}}_{f_{in}} \tag{5}$$

where $\dot{\boldsymbol{S}}_i|_{ex}$ denotes the external dynamics (which stem from the environment) and $\dot{\boldsymbol{S}}_i|_{in}$ the internal ones (which stem from the use of propulsion).

3.1. *External dynamics— f_{ex}*

Then, f_{ex} was selected to comprise the Sun-Earth Circular Restricted Three Body Problem (CR3BP) model f_{ex}^{CR3BP} and the Solar Radiation Pressure (SRP) model f_{ex}^{SRP}; giving: $\dot{\boldsymbol{S}}_i|_{ex} = \dot{\boldsymbol{S}}_i|_{ex}^{\text{CR3BP}} + \dot{\boldsymbol{S}}_i|_{ex}^{\text{SRP}}$, where $\dot{\boldsymbol{S}}_i|_{ex}^{\text{CR3BP}}$ are the dynamics from CR3BP and $\dot{\boldsymbol{S}}_i|_{ex}^{\text{SRP}}$ are those from SRP. Note here that the assumptions of the CR3BP, as well as the exclusion of other major celestial bodies such as Jupiter from f_{ex}, did not influence the resulting $\mathbb{B}$ (note that the required accuracy was 1 km, because the $[\boldsymbol{s}_{ij}]^{\text{km}}$ entries in $\mathbb{B}$ were rounded to whole km).

3.1.1. *Circular restricted three body problem – f_{ex}^{CR3BP}*

The CR3BP is a well known problem that has been extensively covered in literature. Here, only a brief overview of this problem and its dynamics is provided; the interested reader can consult e.g. Szebehely [37] for more information.

The CR3BP describes the motion of a third body of negligible mass under the gravitational influence of two major bodies—the primaries—which move in circular orbits about their common barycentre with a constant angular velocity [37]:

$$f_{ex}^{\text{CR3BP}} \begin{cases} \ddot{x}_i = x_i + 2\dot{y}_i - \dfrac{(1-\mu)(x_i + \mu)}{R_{\odot i}^3} - \dfrac{\mu(x_i - 1 + \mu)}{R_{\oplus i}^3} \\ \ddot{y}_i = y_i - 2\dot{x}_i - \dfrac{(1-\mu)y_i}{R_{\odot i}^3} - \dfrac{\mu y_i}{R_{\oplus i}^3} \\ \ddot{z}_i = -\dfrac{(1-\mu)z_i}{R_{\odot i}^3} - \dfrac{\mu z_i}{R_{\oplus i}^3} \end{cases} \tag{6}$$

and thus $\dot{\boldsymbol{S}}_i|_{ex}^{\text{CR3BP}} = \left[\dot{\boldsymbol{s}}_i, \ddot{\boldsymbol{s}}_i\right]^T|_{ex}^{\text{CR3BP}} = \left[\dot{x}_i, \dot{y}_i, \dot{z}_i, \ddot{x}_i, \ddot{y}_i, \ddot{z}_i\right]^T|_{ex}^{\text{CR3BP}}$ are then the normalised dynamics of the minor body in the synodic coordinate frame $\mathscr{F}_S(X_S, Y_S, Z_S)$; $\mathscr{F}_S$ is a with Earth co-rotating $\mathscr{F}_o$, in which X_S goes through the centre of mass of both the Sun and the Earth at all times, because X_S co-rotates with the centre of mass of Earth; $R_{\odot i}$ and $R_{\oplus i}$ are the distances from the minor body to the centre of mass of the Sun

Table 1
f_{ex} constants [26,40]

$R_{\oplus\odot}$	149.597870700e9	m
$G^{(*)}M_{\odot}$	1.32712440018e20	m^3/s^2
$G^{(*)}M_{\oplus}$	3.986004418e14	m^3/s^2
L	3.839e26	W
c_{light}	299792458	m/s
c_{srp}	1.2	-

(*) G represents the gravitational constant.

and the Earth, respectively:

$$R_{\odot i} = \sqrt{(x_i + \mu)^2 + y_i^2 + z_i^2} \quad R_{\oplus i} = \sqrt{(x_i - 1 + \mu)^2 + y_i^2 + z_i^2}$$

and μ is a mass ratio:

$$\mu = \frac{M_{\oplus}}{M_{\odot} + M_{\oplus}}$$

with $M_{\odot}$ and $M_{\oplus}$ denoting the mass of the Sun and the Earth, respectively. Eq. (6) is normalised with respect to the system's total mass $M_{\odot} + M_{\oplus}$ (which becomes 1 in nondimensional units).

the distance between the primaries $R_{\oplus\odot}$ (which becomes 1 as well) and the orbital period (which becomes 2π). The primaries are modelled as point-masses and are stationary in $\mathscr{F}_S$, in which they have the coordinates $s_{\odot} = [-\mu, 0, 0]^T$ and dst $s_{\oplus} = [1 - \mu, 0, 0]^T$ in nondimensional units from the barycentre. The constants that are used in this work for Eq. (6) are defined in Table 1.

Since Eq. (6) is defined in normalised form and the dynamics of Eq. (5) are propagated as a whole, all states that are fed into Eq. (5) must be normalised as well (in non-normalised form, Eq. (6) looses accuracy due to the 'to the third power' terms in double-precision floating point formats, which have an accuracy of about 16 digits). To transform an acceleration term from the metric dimensional system to the normalised units of CR3BP, the following factor can be used:

$$c_{n/d}^{\ddot{s}} = \frac{R_{\odot\oplus}^2}{GM_{\odot} + GM_{\oplus}} \tag{7}$$

3.1.2. Solar radiation pressure – f_{ex}^{SRP}

The SRP exerts a force that is repulsive with respect to the Sun; in normalised form f_{ex}^{SRP} is [26]:

$$f_{ex}^{SRP}\left\{\ddot{s}_i = -\frac{L}{4\pi R_{\odot i}^2}\frac{A_i\, c_{srp}}{m_i\, c_{light}}\frac{s_{\odot i}}{\|s_{\odot i}\|}c_{n/d}^{\ddot{s}}\right. \tag{8}$$

with which $\dot{S}_i|_{ex}^{SRP} = [\dot{s}_i, \ddot{s}_i]^T|_{ex}^{SRP} = [\dot{x}_i, \dot{y}_i, \dot{z}_i, \ddot{x}_i, \ddot{y}_i, \ddot{z}_i]^T|_{ex}^{SRP}$ is then defined and where L is the solar luminosity, A_i the S/C area that is exposed to the Sun (see Section 4), c_{srp} the satellite's radiation pressure coefficient, c_{light} the speed of light. The constants that are used in this work for Eq. (8) are defined in Table 1.

3.2. Internal dynamics – f_{in}

3.2.1. Poghosyan et al. [31] Define distributed space systems

(DSS), such as swarms, as mission architectures consisting of multiple space elements that interact, cooperate and communicate with each other, usually resulting in new systematic properties and emerging functions. In literature, the different control approaches for DSS have been covered by among others [27,31,33,34]—to which the interested reader is referred to for more information. The control approach that is employed in this work is based on the Virtual Model Reference Adaptive Control (VMRAC) by Ref. [3], which allows the control of relative states S_{ij} to be autonomous and to be performed in a distributed fashion. Note that autonomy has a number of advantages—among others, it can guarantee superior performance with respect to control accuracies (see e.g. Ref. [34]). Distributed control architecture is advantageous as well—it enables the swarm as a whole to be more robust to failures of individual S/C, because it is based on an equal distribution of the leader function over each S/C; the leader function will therefore not be lost if a subset of S/C fails [27]. Additionally, note that Poghosyan et al. [31] mention that the control of a space-based swarm should be distributed equally over the S/C up until t_{end}, to enable the use of identical S/C that include identical amounts of fuel (to allow for cost reduction due to series production of S/C).

3.2.2. VMRAC

In this section, a short summary of the VMRAC state consensus protocol by Baldi and Frasca [3] is provided (see Ref. [3] for a more in depth explanation). Consider a multi-agent, Linear Time Invariant (LTI) Single Input Single Output (SISO) system of N agents, defined by the set $\mathscr{N}$, with initial states $x_i(t_0)$ and dynamics $\dot{x}_i = A_m x_i + b_m u_i$, where $x_i = [x_i, \dot{x}_i]^T$, $\dot{x}_i = [\dot{x}_i, \ddot{x}_i]^T$ and $i \in \mathscr{N} = \{1, 2, \ldots, N\}$. Then, the VMRAC defines the consensus protocol $u_i = f^T \sum_{j=1}^{N} a_{ij}(x_{ij})$—where a_{ij} are the communication links and $x_{ij} = x_j - x_i$ —that can ensure that the states of the agents synchronise to the state of the Virtual Leader (V/L) x_o over time (i.e., $x_i - x_o = x_{oi} \rightarrow 0, \forall i \in \mathscr{N}$) if the following holds: $A_m + \lambda_i b_m f^T$ is Hurwitz, $\forall i \in \mathscr{N}$, where λ_i are the non-zero eigenvalues of the Laplacian matrix $\mathscr{L}$ that can be constructed from the communication matrix $\mathscr{A}$. For clarification, consider the example provided in Fig. 1(I), which depicts a distributed network of $N = 5$ elements. This network has a certain, undirected communication architecture, which can be defined by the communication links a_{ij} for which holds: $a_{ij} = 1$ for a connected link and $a_{ij} = 0$ otherwise (note here that $a_{ij} = a_{ji}$ because the communication is undirected). For this network holds:

$$\mathscr{A} = \begin{bmatrix} 0 & 1 & 1 & 0 & 1 \\ 1 & 0 & 1 & 1 & 0 \\ 1 & 1 & 0 & 1 & 0 \\ 0 & 1 & 1 & 0 & 1 \\ 1 & 0 & 0 & 1 & 0 \end{bmatrix} \quad \mathscr{L} = \begin{bmatrix} 3 & -1 & -1 & 0 & -1 \\ -1 & 3 & -1 & -1 & 0 \\ -1 & -1 & 3 & -1 & 0 \\ 0 & -1 & -1 & 3 & -1 \\ -1 & 0 & 0 & -1 & 2 \end{bmatrix} \tag{9}$$

Note here that $\mathscr{A}(i,j) = a_{ij}$; $\mathscr{L}$ is constructed from $\mathscr{A}$: each diagonal entry of $\mathscr{L}$ is the sum of its respective row in $\mathscr{A}$, and the non-diagonal

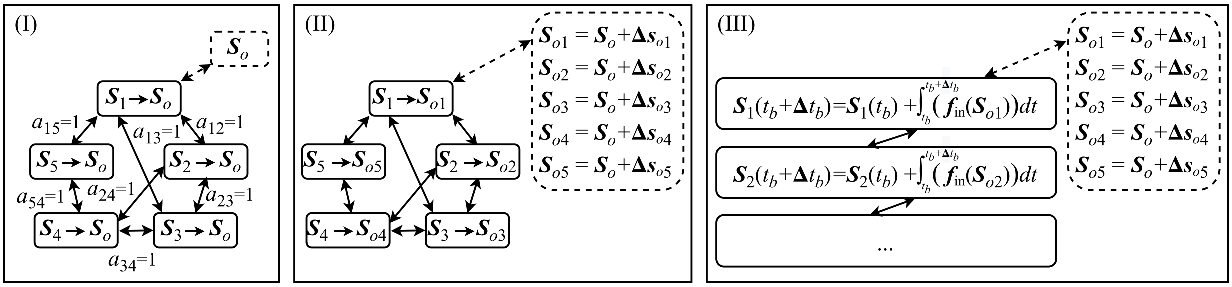

Fig. 1. Examples of distributed control architectures; (I) state consensus to S_o; (II) state consensus to S_{oi}; (III) state consensus to S_{oi} with restricted control effort.

entries of 1 in $\mathscr{A}$ become entries of -1 in $\mathscr{L}$. For more information on how this algorithm works exactly, the interested reader can consult [3].

3.2.3. VMRAC in 3D with restricted control effort

In this section, the adaptations and restrictions are discussed that are incorporated into the original VMRAC (Section 3.2.1), to make the algorithm suitable for deploying the swarm with a restricted propulsion subsystem output.

The original VMRAC consensus protocol can force all $\boldsymbol{S}_i$ of a swarm N, that are under the influence of some dynamics, to reach state consensus over time with respect to the state of the V/L $\boldsymbol{S}_o$, as is depicted in Fig. 1(I): $\boldsymbol{S}_i \rightarrow \boldsymbol{S}_o$; note that this leads to $\|\boldsymbol{s}_{ij}\| \rightarrow 0$. However, to construct the required $\mathbb{B}$ (Eq. (3)), deployment of the swarm is needed ($\|\boldsymbol{s}_{ij}\| \neq 0$), rather than state consensus ($\|\boldsymbol{s}_{ij}\| = 0$). Deployment can be achieved by using VMRAC in which the perceived location of the V/L is changed for each S/C by a vector that is defined w.r.t. the V/L $\Delta\boldsymbol{s}_{oi} = \boldsymbol{s}_i - \boldsymbol{s}_o$, that will force the states of a swarm to reach state consensus at an offset $\Delta\boldsymbol{s}_{oi}$ w.r.t. the V/L, as is depicted in Fig. 1(II): $\boldsymbol{S}_i \rightarrow \boldsymbol{S}_o + \Delta\boldsymbol{s}_{oi}$; note that this can lead to swarm deployment: $\|\boldsymbol{s}_{ij}\| \neq 0$ if $\Delta\boldsymbol{s}_{oi} \neq \Delta\boldsymbol{s}_{oj}$. Then, using $\Delta\boldsymbol{s}_{oi}$ to define the direction of a thrust manoeuvre, the 3D deployment protocol can be defined as:

$$\begin{cases} u_{x,i} = f^T \sum_{j=1}^{N} a_{ij}\left(\boldsymbol{x}_{ij} + \Delta x_{oi}\right) \\ u_{y,i} = f^T \sum_{j=1}^{N} a_{ij}\left(\boldsymbol{y}_{ij} + \Delta y_{oi}\right) \\ u_{z,i} = f^T \sum_{j=1}^{N} a_{ij}\left(z_{ij} + \Delta z_{oi}\right) \end{cases} \tag{10}$$

The original VMRAC, as defined in Section 3.2.1, does not account for a restriction of the control effort u_i. However, for a CubeSat, u_i is restricted by hardware characteristics of the propulsion subsystem, in terms of l$F_{T,i}$ and $T_{b,i}$ (see Section 4), and additionally depends on m_i; more specifically, the following relation must be upheld: $\left\| \ddot{\boldsymbol{s}}_i \right\| \Big|_{in} = \sqrt{\ddot{x}_i^2 + \ddot{y}_i^2 + \ddot{z}_i^2}\Big|_{in} = F_{T,i}/m_i$. Furthermore, $\boldsymbol{f}_{in}$ must be made congruent with the units of $\boldsymbol{f}_{ex}$. Incorporation of these aspects gives the resulting $\boldsymbol{f}_{in}$:

$$\boldsymbol{f}_{in} \begin{cases} \ddot{x}_i = \dfrac{u_{x,i}}{\|\boldsymbol{u}_i\|} \dfrac{F_{T,i}}{m_i} {c_{n/d}}^{\ddot{s}} \\ \ddot{y}_i = \dfrac{u_{y,i}}{\|\boldsymbol{u}_i\|} \dfrac{F_{T,i}}{m_i} {c_{n/d}}^{\ddot{s}} \\ \ddot{z}_i = \dfrac{u_{z,i}}{\|\boldsymbol{u}_i\|} \dfrac{F_{T,i}}{m_i} {c_{n/d}}^{\ddot{s}} \end{cases} \tag{11}$$

where $\|\boldsymbol{u}_i\| = \sqrt{u_{x,i}^2 + u_{y,i}^2 + u_{z,i}^2}$; $\dot{\boldsymbol{S}}_i\Big|_{in} = [\dot{\boldsymbol{s}}_i, \ddot{\boldsymbol{s}}_i]_{in}^T = [\dot{x}_i, \dot{y}_i, \dot{z}_i, \ddot{x}_i, \ddot{y}_i, \ddot{z}_i]_{in}^T$ is then defined.

4. Hardware parameters

The parameters m_i and A_i in Eq. (8), and $F_{T,i}$ in Eq. (11), can be defined by inspecting the hardware characteristics of CubeSat subsystems that are considered for the mission.

As mentioned previously in Section 1, one of the core goals of this work is to test whether the mission objectives (defined by $\mathbb{B}$ in Eq. (3)) can be reached in a cost effective manner. Since mission cost is significantly influenced by the total mission mass M_{swarm} that must be launched, the objective becomes thus to reduce M_{swarm}, which is defined as:

$$M_{swarm} = N\left(M_{OS,i} + M_{PS,i}\right) \tag{12}$$

Table 2
Hardware parameters.

Case	1/2/4	U	Case	1	2	4	U
$M_{OS,i}$	4	kg	$M_{PS,i}$	2	4	8	kg
$\dot{m}_{f,i}$	1.8*e*-4	kg/s	$T_{b,i}$	1700	3740	8228	s
$F_{T,i}$	0.5	N					
A_i	0.36	m					

where $M_{PS,i}$ is the wet mass of the propulsion subsystem and $M_{OS,i}$ is the mass of all subsystems excluding $M_{PS,i}$.

With $M_{OS,i}$ assumed to be fixed, two parameters remain that can be adapted in Eq. (12) to influence M_{swarm}, namely N and $M_{PS,i}$. Then, the following assumptions are made. For each S/C i, the total mass of all subsystems excluding the propulsion subsystem $M_{OlS,i} = 4$ kg (based on the works of [32,33,35]). Additionally, each S/C shall have a propulsion subsystem (with fuel included) of mass $M_{PS,i}$, for which three different cases are considered: $M_{PS,i}^{1U} = 2$ kg, $M_{PS,i}^{2U} = 4$ kg and $M_{PS,i}^{4U} = 8$ kg, with total available burn time of $T_{b,i}^{1U} = 1700$ s, $T_{b,i}^{2U} = 3740$ s and $T_{b,i}^{4U} = 8228$ s, for propulsion subsystem sizes of 1U, 2U and 4U, respectively (based on the characteristics of the PM200 propulsion system, see Ref. [41]). The instantaneous mass of a S/C m_i is then defined as [48]:

$$m_i(t) = M_{OS,i} + M_{PS,i} - \int_{t_0}^{\Delta T_b(t)} \dot{m}_{f,i} dt \tag{13}$$

where $\dot{m}_{f,i}$ is the fuel mass flow rate, that can be computed from the specific impulse $I_{sp,i} = 285$ s and the nominal thrust $F_{T,i} = 0.5$ N for the PM200: $\dot{m}_{f,i} = F_{T,i}/g_0 I_{sp,i} = 1.8e{-}4$ kg/s, where $g_0 = 9.80665$ m/s^2 is the gravity constant at Earth's surface [48]; $\Delta T_b(t)$ is the total time that the propulsion system has been activated at time t since t_0. Lastly, the assumption is made that $A_i = 0.36$ m^2 for each case. An overview of the hardware parameters is provided in Table 2.

5. Reducing the total swarm mass

The total mission cost can be reduced by reducing M_{swarm}, which depends on N, $M_{OS,i}$ and $M_{PS,i}$ (see Section 4). In this section, the values of two parameters are identified, by means of a global optimisation method, that both contribute to reducing M_{swarm}.

Simulations and optimisations were performed using Matlab [42] and its built-in tool patternsearch [43] (a global optimisation method). Propagation was performed using 'ode23tb' with absolute and relative tolerances set to double precision machine epsilon $= 2^{-52} \approx 2.22 \times 10^{-16}$ (see e.g. Ref. [20] for more information on machine epsilon and computational accuracy). Note that 'ode23tb' is a built-in, implicit, Runge-Kutta integration method and is Matlab's implementation of the more commonly known Trapezoidal Rule and Backward Differentiation Formula of order 2 (TR-BDF2) [4,22]. Computational resources comprised the 'Thales' server of the Space Engineering Department of Delft University of Technology (TU Delft), more specifically: Dell Poweredge R430, which has 56 CPU cores—Intel(R) Xeon(R) CPU E5-2683 v3 @ 2.00 GHz—and a total of 64 Gb of memory.

5.1. Minimising $M_{OS,i}$ by reducing maximum telemetry range

Although the value of $M_{OS,i}$ is assumed to be constant in this work, in reality, it will depend on among others the mass of the power subsystem for telemetry. By reducing the maximum telemetry range, $M_{OS,i}$ and consequently M_{swarm} can be reduced.

5.1.1. Cost function

Consider a S/C 'o' that is propagated using only $\boldsymbol{f}_{ex}$, from an initial state $\boldsymbol{S}_o(t_0)$ for the duration of $T_{ops} = 1$ year, whose ephemeris is stored

Table 3

Optimised $\boldsymbol{S}_o(t_0)$ (Eq. (16)) in $\mathscr{F}_S$, in nondimensional units.

Axes	$s_o(t_0)$ [−]	$\dot{s}_o(t_0)$ [−]
X_S	$-972.848226106772e$-3	$5.74779804244613e$-3
Y_S	$30.8225630496502e$-3	$-48.9754918730614e$-3
Z_S	$4.11824301986062e$-3	$39.9296398877521e$-3

in $\mathbb{S}_o$:

$$\mathbb{S}_o = [\,\boldsymbol{S}_o(t_0) \quad \boldsymbol{S}_o(t_0+\Delta t) \quad \ldots \quad \boldsymbol{S}_o(t_{end})\,] \tag{14}$$

from which the set of distances from S/C ‘o’ to the centre of mass of Earth $\mathbb{R}_{\oplus o}$ can be derived, i.e. $\mathbb{S}_o \vdash \mathbb{R}_{\oplus o}$:

$$\mathbb{R}_{\oplus o} = [\,R_o(t_0) \quad R_o(t_0+\Delta t) \quad \ldots \quad R_o(t_{end})\,] \tag{15}$$

where $R_{\oplus o}(t) = s_o(t) - s_\oplus(t)$. Then, an initial state $\boldsymbol{S}_o(t_0)$ can be found that will reduce the maximum achieved $R_\oplus \in \mathbb{R}_{\oplus o}$, whilst accounting for condition (f) in Eq. (3), by minimising the cost function $J(\boldsymbol{S}_o(t_0))$:

$$J(\boldsymbol{S}_o(t_0)) = \underbrace{\max\{R_{\oplus o}(t) \in \mathbb{R}_{\oplus o}\}}_{\text{reduce } M_{OS,i}} \times \underbrace{\left(n\{R_{\oplus o}(t) \in \mathbb{R}_{\oplus o} \mid R_{\oplus o}(t) < 5 \times 10^6 \text{ km}\} + 1\right)}_{\text{Eq.(3)(d)}} \tag{16}$$
$$\text{whilst } \boldsymbol{S}_o(t_0) \vdash R_{\oplus o}(t_0) = 5 \times 10^6 \text{ km}$$

where $n\{R_{\oplus o}(t) \in \mathbb{R}_{\oplus o} | R_{\oplus o}(t) < 5 \times 10^6 \text{km}\}$ is the number of elements $R_{\oplus o}(t) \in \mathbb{R}_{\oplus o}$ that do not comply with condition Eq. (3)(d). Furthermore, $\boldsymbol{S}_o(t_0)$ in Eq. (16) must be selected such that $R_{\oplus o}(t_0)$ is equal to 5×10^6km (see Eq. (3)(d)).

5.1.2. Results

Then, $J(\boldsymbol{S}_o(t_0))$ in Eq. (16) was minimised, where the elements of $\mathbb{S}_o$ in Eq. (14) were stored on time intervals $\Delta t = 300$ s. The resulting $\boldsymbol{S}_o(t_0)$, in the normalised $\mathscr{F}_S$, is provided in Table 3, which gave $\max\{R_{\oplus o}(t) \in \mathbb{R}_{\oplus o}\} \approx 8.7 \times 10^6$km. The corresponding orbit, which is referred to as the ‘design’ or ‘nominal’ orbit, is depicted in Fig. 2 (propagated for two years to illustrate behaviour).

5.1.3. Discussion

For rough benchmarking purposes, the orbit of the Kepler Space Telescope (KST) is plotted as well in Fig. 2. Here, it is plotted twice: once using the KST ephemeris as provided by NASA [44]; and once using only the initial state for KST from NASA [44], and propagating it using $\boldsymbol{f}_{ex}$ (for validation). Fig. 2 shows that KST drifted $\sim 15 \times 10^6$ km from Earth per year. Compared to KST, the design orbit found using $J(\boldsymbol{S}_o(t_0))$ in Eq. (16), had a larger offset in Z_S -axis from the $\{X_S, Y_S\}$ - plane than KST had. During optimisation, this trend was observed as well: a larger offset Z_S -axis offset from the $\{X_S, Y_S\}$ -plane can reduce $\max\{R_{\oplus o}(t) \in \mathbb{R}_{\oplus o}\}$. Compared to KST, that thus drifted $\sim 15 \times 10^6$ km from Earth per year, with the found $\boldsymbol{S}_o(t_0)$, the swarm’s maximum required telemetry range $\max\{R_{\oplus o}(t) \in \mathbb{R}_{\oplus o}\}$ was reduced to a mere $\sim 8.7 - 5 = \sim 3.7 \times 10^6$km for $T_{ops} = 1$ year.

5.2. Minimising mission mass regarding N and $M_{PS,i}$

Then, the objective is to find the combination of N and $M_{PS,i}$ that gives a preliminary minimal M_{swarm} (not the absolute minimal per se; here, not an optimal, but a good enough solution is sought—because the design space is large, finding an optimal solution is challenging and is considered to be out of scope in this work), whilst still meeting the mission objective $\mathbb{B}$ (Eq. (3)). This can be done by finding a $\mathbb{D}_{\mathscr{N}}(\Delta\boldsymbol{s})$, for a number of possible combinations of N and $M_{PS,i}$, that provides a preliminary best result regarding $\mathbb{B}$ (Eq. (3)). These results can then be compared; the combination of N and $M_{PS,i}$ that gives a minimal M_{swarm} and meets $\mathbb{B}$ (Eq. (3)) can then be considered as a preliminary best solution, from which a preliminary M_{swarm} estimation can be derived. Note that the release form launcher and the initial acquisition phase are not considered here.

5.2.1. Cost function

Consider the swarm $\mathscr{N}$ that is propagated using $\boldsymbol{f}_{ex} + \boldsymbol{f}_{in}$ (Eq. (6), (8) and (11)) from $\boldsymbol{S}_i(t_0) = \boldsymbol{S}_o(t_0)$ (see Table 3) $\forall i \in \mathscr{N}$, for the duration of $T_{ops} = 1$ year, whose ephemeris is stored in $\mathbb{S}_{\mathscr{N}}$:

$$\mathbb{S}_{\mathscr{N}} = \begin{bmatrix} \boldsymbol{S}_1(t_0) = \boldsymbol{S}_o(t_0) & \boldsymbol{S}_1(t_0+\Delta t) & \cdots & \boldsymbol{S}_1(t_{end}) \\ \boldsymbol{S}_2(t_0) = \boldsymbol{S}_o(t_0) & \boldsymbol{S}_2(t_0+\Delta t) & \cdots & \boldsymbol{S}_2(t_{end}) \\ \vdots & \vdots & \ddots & \vdots \\ \boldsymbol{S}_N(t_0) = \boldsymbol{S}_o(t_0) & \boldsymbol{S}_N(t_0+\Delta t) & \cdots & \boldsymbol{S}_N(t_{end}) \end{bmatrix} \tag{17}$$

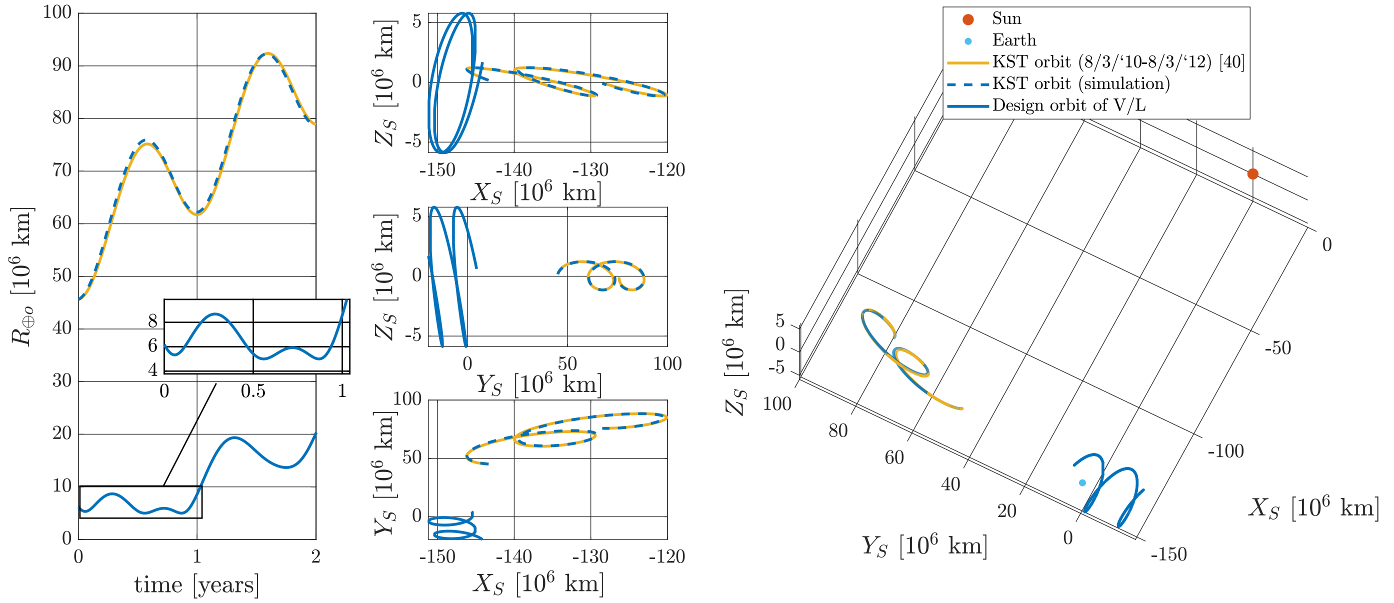

Fig. 2. Nominal swarm orbit (i.e., without the use of fuel, in solid blue) for $T_{ops} = 1$ year, obtained from $J(\boldsymbol{S}_0(t_0))$ in Eq. (16). (For interpretation of the references to colour in this figure legend, the reader is referred to the Web version of this article.)

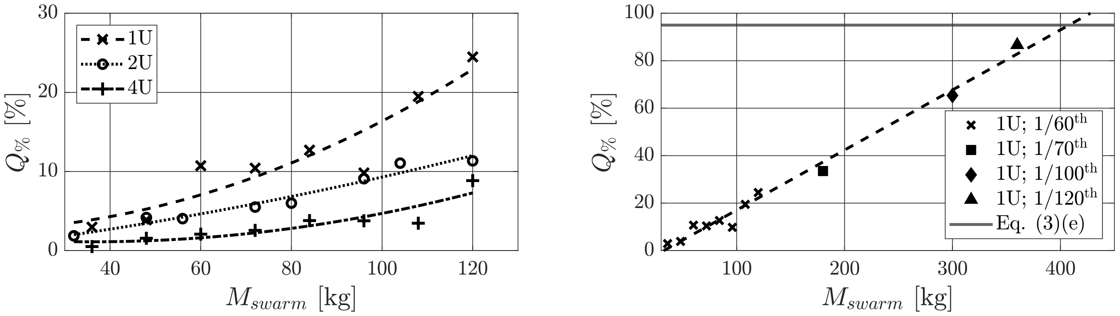

Fig. 3. Resulting preliminary maximised coverage $Q\%$ as a function of M_{swarm}.

from which the set of distances from S/C i, $\forall i \in \mathcal{N}$, to the centre of mass of Earth $\mathbb{R}_{\oplus\mathcal{N}}$ can be derived, i.e. $\mathbb{S}_{\mathcal{N}} \vdash \mathbb{R}_{\oplus\mathcal{N}}$:

$$\mathbb{R}_{\oplus\mathcal{N}} = \begin{bmatrix} R_{\oplus 1}(t_0) & R_{\oplus 1}(t_0+\Delta t) & \cdots & R_{\oplus 1}(t_{end}) \\ R_{\oplus 2}(t_0) & R_{\oplus 2}(t_0+\Delta t) & \cdots & R_{\oplus 2}(t_{end}) \\ \vdots & \vdots & \ddots & \vdots \\ R_{\oplus N}(t_0) & R_{\oplus N}(t_0+\Delta t) & \cdots & R_{\oplus N}(t_{end}) \end{bmatrix} \tag{18}$$

where $R_{\oplus i}(t) = s_i(t) - s_{\oplus}(t)$, $\forall i \in \mathcal{N}$. Then, a collection of thrust manoeuvre directions DN(Δs) can be found, that are defined with respect to S/C 'o' (the design or nominal orbit, see Section 5.1) that serve as inputs in f_{in} (Eq. (11)):

$$\mathbb{D}_{\mathcal{N}}(\Delta \boldsymbol{s}) = \begin{bmatrix} \Delta \boldsymbol{s}_{o1}(t_{b1}) & \Delta \boldsymbol{s}_{o1}(t_{b2}) & \cdots & \Delta \boldsymbol{s}_{o1}(t_{b,last}) \\ \Delta \boldsymbol{s}_{o2}(t_{b1}) & \Delta \boldsymbol{s}_{o2}(t_{b2}) & \cdots & \Delta \boldsymbol{s}_{o2}(t_{b,last}) \\ \vdots & \vdots & \ddots & \vdots \\ \Delta \boldsymbol{s}_{oN}(t_{b1}) & \Delta \boldsymbol{s}_{oN}(t_{b2}) & \cdots & \Delta \boldsymbol{s}_{oN}(t_{b,last}) \end{bmatrix} \tag{19}$$

(where $\{t_{b1}, t_{b2}, \ldots, t_{b,last}\}$ denote the successive times at the start of the burn manoeuvres) that will increase the achieved coverage (i.e. aim to comply with the mission objective Eq. (3)(e)) and (further) reduce the maximum achieved $R_{\oplus i}(t) \in \mathbb{R}_{\oplus\mathcal{N}}(t)$, $\forall i \in \mathcal{N}$, whilst complying with the imaging conditions (Eq. (3)(a-d)):

$$J(\mathbb{D}_{\mathcal{N}}(\psi,\theta)) = \underbrace{\frac{Q_{max}}{q}}_{\text{Eq.(3)(e)}} \left(\underbrace{\frac{\max\{R_{\oplus i}(t) \in \mathbb{R}_{\oplus\mathcal{N}}\}}{\max\{R_{\oplus o}(t) \in \mathbb{R}_{\oplus o}\}}}_{\text{reduce } M_{OS,i}} \right) \times \underbrace{\text{penalty}}_{\text{Eq.(3)(d)}} \tag{20}$$

$$\text{penalty} \begin{cases} 100 & \text{if } \min\{R_{\oplus i}(t) \in \mathbb{R}_{\oplus\mathcal{N}}\} < 5 \times 10^6 \text{ km} \\ 1 & \text{else} \end{cases}$$

$$q = n\{\boldsymbol{S}_{ij} \in \mathbb{B} \mid \text{Eq.(3)(a} - \text{c)}\}$$

where $\max\{R_{\oplus o}(t) \in \mathbb{R}_{\oplus o}\} = 8.7 \times 10^6$km (see Section 5.1.2); q is the number of elements $\boldsymbol{S}_{ij} \in \mathbb{B}$ that comply with conditions of Eq. (3)(a-c). To reduce the number of optimisation parameters, each $\Delta \boldsymbol{s}_{oi}$ in Eq. (19) can be defined by 2 angles, $0 \le \psi \le 360$ deg and $0 \le \theta \le 180$ deg, and one assumed length; this length is taken as 1 in normalised units; $\mathbb{D}_{\mathcal{N}}(\Delta \boldsymbol{s})$ then reduces to:

$$\mathbb{D}_{\mathcal{N}}(\psi,\theta) = \begin{bmatrix} \psi_1(t_{b1}) & \psi_1(t_{b2}) & \ldots & \psi_1(t_{b,last}) \\ \theta_1(t_{b1}) & \theta_1(t_{b2}) & \ldots & \theta_1(t_{b,last}) \\ \psi_2(t_{b1}) & \psi_2(t_{b2}) & \ldots & \psi_2(t_{b,last}) \\ \theta_2(t_{b1}) & \theta_2(t_{b2}) & \ldots & \theta_2(t_{b,last}) \\ \vdots & \vdots & \ddots & \vdots \\ \psi_N(t_{b1}) & \psi_N(t_{b2}) & \ldots & \psi_N(t_{b,last}) \\ \theta_N(t_{b1}) & \theta_N(t_{b2}) & \ldots & \theta_N(t_{b,last}) \end{bmatrix} \tag{21}$$

Additionally, for further reduction of design space, the burn manoeuvres for each S/C $i \in \mathcal{N}$, for each case of thruster subsystem size, were performed synchronously; i.e., they had the same start time t_b and duration for each burn Δt_b; additionally, they were spread with equal intervals throughout T_{ops}, where for the start time of the first burn the following holds: $t_{b1} = t_0$.

To alleviate computational burden further, simplifications in the communication topology are adapted. First, the communication flow in simulations is modelled as time-invariant. Second, each S/C is modelled to communicate only with its direct neighbours and only the first S/C has direct access to the V/L state (which is the nominal orbit), e.g. for an N S/C system the following coordination topology holds: $o - 1 - 2 - \ldots - N$; here, 'o' denotes the V/L, '$\{1, 2, \ldots, N\}$' the set of S/C and '$-$' the communication links (see Fig. 1(III)).

Lastly, the design space was further reduced by considering symmetry properties, by which the term $\frac{Q_{max}}{q}$ (in Eq. (20)) becomes $\frac{Q_{max}/2}{q_{\text{non-sym}}}$, where for $q_{\text{non-sym}}$ holds that $\boldsymbol{s}_{ij} = \boldsymbol{s}_{ji}$ are counted as one unique baseline (see e.g. Refs. [15,33] for more explanation on these symmetry properties).

5.2.2. Results

Then, $J(\mathbb{D}_{\mathcal{N}}(\psi,\theta))$ in Eq. (20) was minimised, where the elements of $\mathbb{S}_{\mathcal{N}}$ (Eq. (17)) were stored on time intervals $\Delta t = 300$ s during non-actuation and in un-adjusted form during actuation (of which the stored ephemeris was defined by the integrator and its settings). The resulting $\mathbb{S}_{\mathcal{N}}$ gave $\max\{R_{\oplus i}(t) \in \mathbb{R}_{\oplus\mathcal{N}}\} \approx 6.6 \times 10^6$km. The resulting coverage $Q_{\%}$ is plotted against M_{swarm} in Fig. 3. For M_{swarm} of up to 120 kg, for each of the three $M_{PS,i}$ cases (1U, 2U and 4U, see Section 4), $J(\mathbb{D}_{\mathcal{N}}(\psi,\theta))$ was optimised in chunks of 1/60th of a year—which was necessary to enable the optimisations with the available computational resources (i.e., some of the scenarios of up to 120 kg could not be optimised in larger temporal chunks as the computational resources ran out of memory and the optimisation processes would terminate). The durations of burn manoeuvres Δt_b that were used were 0.15 s, 0.15 s and 0.20 s for $M_{PS,i}$ cases of 1U, 2U and 4U, respectively, as these showed favourable trends. These results are shown in the left plot of Fig. 3, where the underlying trends are revealed by fitting a second order polynomial through the data points. The trends imply that, for a given launch mass, the 1U case can provide a higher coverage. However, none of the scenarios up to 120 kg are able to provide the required coverage of 95%—i.e., optimisations with larger swarm sizes are required. However, optimisations with larger swarm sizes were not possible on temporal sections of 1/60th of a year, since the computational resources ran out of memory. The duration of an optimisation section had to be decreased to 1/70th, 1/100th and 1/120th of a year for 30, 50 and 60 S/C, respectively. For this reason, the curve in the right plot is obtained using linear regression, since the results here cannot be fairly compared (it is assumed here that the results obtained on sections of 1/60th have a higher probability of finding a better solution than the results obtained with smaller sections). As can be seen in the right plot in Fig. 3, the coverage requirement of 95 % (see Eq. (3)(e)) can be met with $M_{swarm} = 402$ kg, i.e. $N = 68$ S/C for a 1U thruster subsystem.

Note that a second polynomial was selected to fit through the data points in the left plot of Fig. 3 based on the following reasoning. The coverage $Q_{\%}$ is directly proportional to the number of unique baseline q (or $q_{\text{non-sym}}$) that is achieved by the swarm throughout the operational

Table 4
Coverage optimisation settings.

Characteristic	Setting
Optimiser	Pattern search
Search function	Latin hypercubes
Poll function	'MADSPositiveBasis2N'
'PollOrderAlgorithm'	'success'
Lower bound $\{\psi, \theta\}$	{0, 0} deg
Upper bound $\{\psi, \theta\}$	{360, 180} deg
Initial mesh size	180 deg
Final mesh size	1 deg
'AccelerateMesh'	'on'
Maximum number of function evaluations	20 60 (for up to 120 kg);
Number of temporal optimisation sections in 1 year	{70, 100, 120} for {30, 50, 60} S/C (1U)
Duration of individual burn manoeuvres Δt_b	{0.15, 0.15, 0.20} s for {1, 2, 4} U

life ($Q_{\%} = \frac{q}{Q_{max}} \times 100\%$, see Section 1). In turn, q is approximately directly proportional to the total number of non-unique baselines at a point in time $K_{baselines}(t) = N(N-1)$ (or $K_{baselines}(t) = 0.5N(N-1)$ if $q_{\text{non-sym}}$ is considered) (because q is essentially the sum of $K_{baselines}(t)$ over T_{ops} that complies with a set of conditions, see Eq. (3)). In summary:

$$Q_{\%} \propto q \propto K_{baselines}(t) = N^2 - N \tag{22}$$

Additionally, from Eq. (12), the following relation can be derived: $N \propto M_{swarm}$; which together with Eq. (22), can reveal the expected relation between $Q\%$ and M_{swarm}:

$$Q_{\%} \propto \sim M_{swarm}^2 - M_{swarm} \tag{23}$$

The results were obtained using Matlab's built-in tool patternsearch, of which the settings are provided in Table 4. These settings were selected as they showed favourable trends regarding the optimisation results as well as the computational time. The initial guess for $\mathbb{D}_{\mathcal{N}}(\psi, \theta)$ at $t = t_{b1}$ (Eq. (21)) was generated randomly with generator 'twister' with seed '0' [45]. The optimisation for each section (each section of time that is optimised separately and successively), for each case of N and $M_{PS,i}$, was performed in 5 iterations, with each next iteration using the previous solution as input.

For visualisation purposes, the motion of the S/C is provided relative to their mean centre $[x_{avg,i}(t), y_{avg,i}(t), z_{avg,i}(t)]$, where $x_{avg,i}(t) = x_i(t) - x_{avg}(t)$ and $x_{avg}(t) = 1/N \sum_{i=1}^{i=N} x_i(t)$, in $\mathscr{F}_S$ for $t = 0$ year to $t = 1/120$ year, in Fig. 4.

5.2.3. Discussion

The obtained results comply with the mission objective as defined in Section 1 and summarised in Eq. (3). Compared to the results of Dekens et al. [15], the results obtained in this work required a smaller number of S/C ($\sim$ 68 instead of $\sim$100) to meet $Q_{\%} \geq 95$ %. Additionally, the obtained results complied with the relative baseline speed requirement (see Eq. (3)(b)); the HELO is therefore deemed suitable. The main concern regarding selecting HELO as the operational orbit was the maximum telemetry range required for the swarm, since in this orbit this range can increase $\sim 15 \times 10^6$ km on a year basis, as was seen in Fig. 2 for KST. However, after performing preliminary optimisations this range was significantly reduced. Using a 1U propulsion subsystem and an optimised initial state $S_{ij}(t_0)$, the thrust manoeuvres can be performed in such a way that the maximum telemetry range is reduced to a mere 6.6 $\times 10^6$ km (instead of the initially expected $\sim 5 + 15 = 20 \times 10^6$ km).

6. Discussion

The presented orbit solution shows that the mission objective—mapping the full sky in the ULW regime in 3D—can be met with 68 S/C. The total launch mass, that is dependent among others on the swarm size and the power subsystem for telemetry, can be reduced by optimising the directions of the executed thrust manoeuvres and by reducing the maximum drift from Earth. The proposed orbit solution shows an improvement regarding previously proposed solutions, e.g. by Ref. [15], regarding the swarm size, as well regarding complying with the imposed imaging conditions, more specifically with the baseline speed requirement of ≤3 m/s.

Due to the framework of assumptions and simplifications that are applied in this work, a precise prediction of the actual swarm launch mass is still out of reach. However, this work shows promising results in

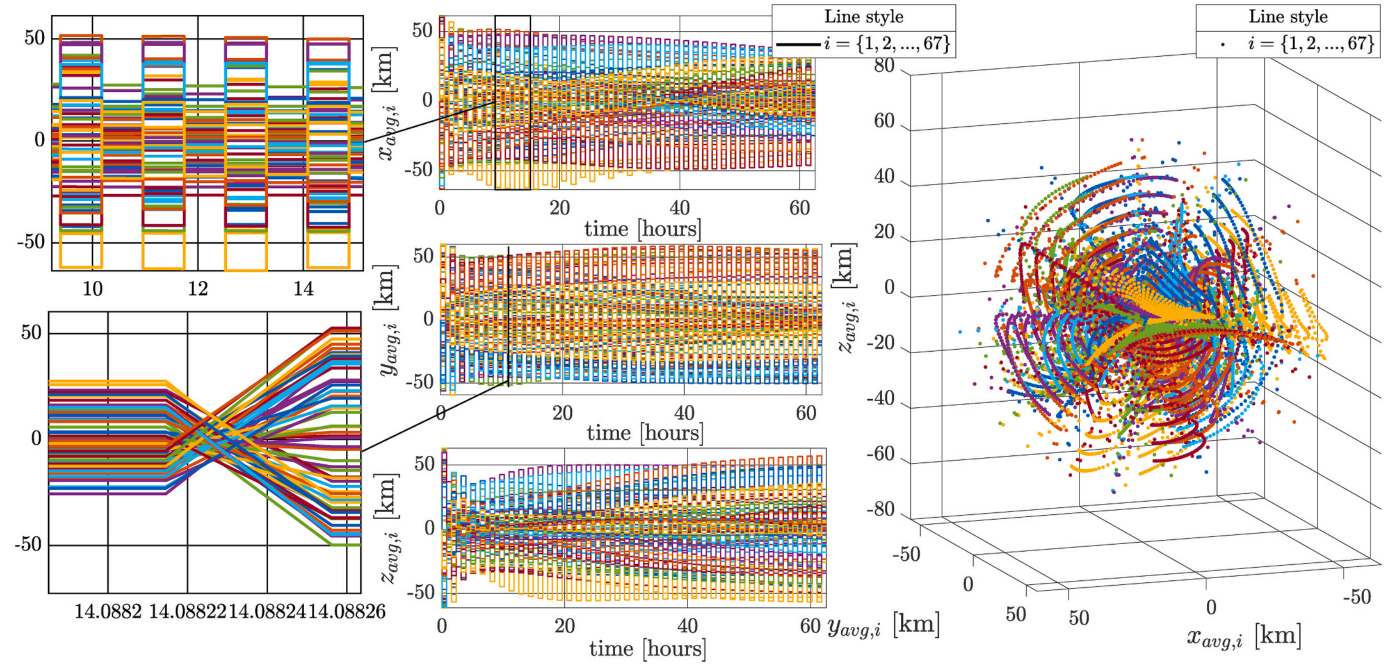

Fig. 4. Motion of the S/C relative to their mean centre $[x_{avg,i}(t), y_{avg,i}(t), z_{avg,i}(t)]$.

the proposed orbit solution, in which there have been found no significant drawbacks (except perhaps for the level of complexity). This work can serve as a benchmark for future work in which more sophisticated solutions can be explored. For a more precise estimation of the swarm launch mass, among others a more exact estimation of $M_{OS,i}$ would be required, for which the in this work found maximum telemetry range can serve as a guideline for power subsystem sizing for telemetry (i.e., the design can be performed in an iterative way). Additionally, for a more precise estimation of the swarm launch mass, the integration of the full Guidance, Navigation and Control (GNC) solution can be considered, which should include the estimated errors and deviations in the GNC hardware and software, as well as an estimation of expected faults and failures, with accompanying set of mitigation solutions (e.g., including redundant S/C). Note that making a prediction of the failure rate is not achievable at this point in time (and therefore, neither is the estimation of the required number of redundant S/C which will allow to maintain the designed level of swarm performance), as it will majorly depend on the design of the spacecraft. The importance of failure mitigation solution should not be underestimated: a S/C that is faulty, can negatively affect the performance of the entire swarm (e.g., a rogue S/C could collide with other S/C). To prevent this, previously, it has been proposed to incorporate either a form of S/C apoptosis or ex-communication [16,21]. In apoptosis, a S/C should be able to detect its own faults and either reboot or remove itself from the swarm network in terms of communication (or even physically). In ex-communication, the other healthy S/C should be able to detect the faulty S/C and either make it reboot or disregard its communication signals in their decision logic (thus simply stop 'listening' to it).

7. Conclusion

The importance of enabling the creation of a map of the sky in the ULW regime is arguably undeniable. However, the amount of proposed as well as analysed orbit solutions to this end has thus far, unfortunately, remained limited. The results found in this work are promising. However, more research is needed to benchmark these results against possible solutions in perhaps different orbits, as well as to perform a more detailed full system analysis.

With the recent advancements in technology, realising a ULW swarm seems not only achievable, but perhaps even affordable.

Declaration of competing interest

The authors declare that they have no known competing financial interests or personal relationships that could have appeared to influence the work reported in this paper.

References

[1] J.K. Alexander, M.L. Kaiser, J.C. Novaco, F.R. Grena, R.R. Weber, Scientific instrumentation of the radio-astronomy-explorer-2 satellite, Astron. Astrophys. 40 (1975) 365–371.

[2] A. Aminaei, M. Klein-Wolt, L. Chen, T. Bronzwaer, H.R. Pourshaghaghi, M. J. Bentum, H. Falcke, Basic radio interferometry for future lunar missions, in: IEEE Aerospace Conference, IEEE, 2014, pp. 1–19. https://doi.org/10.1109/AERO.2014.6836271}.

[3] S. Baldi, P. Frasca, Adaptive synchronization of unknown heterogeneous agents: an adaptive virtual model reference approach, J. Franklin Inst. 356 (2019) 935–955. https://doi.org/10.1016/j.jfranklin.2018.01.022}.

[4] R.E. Bank, W.M. Coughran, W. Fichtner, E.H. Grosse, D.J. Rose, R.K. Smith, Transient simulation of silicon devices and circuits, IEEE Trans. Comput. Aided Des. Integrated Circ. Syst. 4 (1985) 436–451.

[5] M.J. Bentum, A.J. Boonstra, The RFI situation for a space-based low-frequency radio astronomy instrument, in: 2016 Radio Frequency Interference (RFI), IEEE, IEEE Antennas and Propagation Society, 2016, pp. 1–6. https://doi.org/10.1109/RFINT.2016.7833521}.

[6] M.J. Bentum, C.J.M. Verhoeven, A.J. Boonstra, A.J. van der Veen, E.K.A. Gill, A novel astronomical application for formation flying small satellites, in: 60th International Astronautical Congress, 2009, pp. 1–8.

[7] M.J. Bentum, M.K. Verma, R.T. Rajan, A.J. Boonstra, C.J.M. Verhoeven, E.K.A. Gill, A.J. van der Veen, H. Falcke, M.K. Wolt, B. Monna, S. Engelen, J. Rotteveel, L. I. Gurvits, A roadmap towards a space-based radio telescope for ultra-low frequency radio astronomy, Adv. Space Res. 65 (2019) 856–867. https://doi.org/10.1016/j.asr.2019.09.007.

[8] J.E.S. Bergman, R.J. Blott, A.B. Forbes, D.A. Humphreys, D.W. Robinson, C. Stavrinidis, FIRST explorer – an innovative low-cost passive formation-flying system, in: CEAS 2009 – European Air & Space Conference, 2009, pp. 1–14, arXiv preprint arXiv:0911.0991.

[9] A.J. Boonstra, N. Saks, M.J. Bentum, H. Falcke, M. Klein-Wolt, R.T. Rajan, S. J. Wijnholts, M. Arts, K. vant Klooster, F. Belien, DARIS, A low-frequency distributed aperture array for radio astronomy in space, in: 61th International Astronautical Congress, IAC 2010, IAC, 2010.

[10] L. Buinhas, K. Frankl, H. Linz, R. Forstner, Irassi infrared spacë interferometer: formation geometry and relative dynamics analysis, Acta Astronaut. 153 (2018) 394–409.

[11] J. Burns, R. Bradley, K. Tauscher, et al., A space-based observational strategy for characterizing the first stars and galaxies using the redshifted 21-cm global spectrum, Astrophys. J. 844 (2017) 33.

[12] J. Burns, D. Kring, J. Hopkins, S. Norris, T. Lazio, J. Kasper, A lunar L2- far side exploration and science mission concept with the Orion Multi-Purpose Crew Vehicle and a teleoperated lander/rover, Adv. Space Res. 52 (2013) 306–320.

[13] B. Cecconi, M. Dekkali, C. Briand, B. Segret, J. Girard, A. Laurens, A. Lamy, D. Valat, M. Delpech, M. Bruno, NOIRE study report: towards a low frequency radio interferometer in space, in: 2018 IEEE Aerospace Conference, IEEE, Institute of Electrical and Electronics Engineers, 2018, pp. 1–19. https://doi.org/10.1109/AERO.2018.8396742}.

[14] A. Datta, R. Bradley, J. Burns, G. Harker, A. Komjathy, T. Lazio, Effects of the ionosphere on ground-based Detection of the global 21-cm signal from the cosmic Dawn and the dark ages, Astrophys. J. 831 (2016) 6.

[15] E. Dekens, S. Engelen, R. Noomen, A satellite swarm for radio astronomy, Acta Astronaut. 102 (2014) 321–331. https://doi.org/10.1016/j.actaastro.2013.11.033}.

[16] S. Engelen, E.K. Gill, C.J. Verhoeven, Systems engineering challenges for satellite swarms, in: 2011 Aerospace Conference, IEEE, 2011, pp. 1–8.

[17] G.G. Getmantsev, V.L. Ginzburg, I.S. Shklovskii, Radio astronomical investigations with the aid of artificial satellites, Sov. Phys. Usp. 1 (1958) 65–67. https://doi.org/10.1070/PU1958v001n01ABEH003084}.

[18] S. Gorgolewski, Lunar radio astronomy observatory, in: Proceeding of the First Lunar International Laboratory (LIL) Symposium Research in Geosciences and Astronomy, 1966, pp. 78–84. https://doi.org/10.1007/978-3-662-25087-7_8}.

[19] F.T. Haddock, Radio astronomy observations from space, ARS J. 30 (1960) 598–602. https://doi.org/10.2514/8.5168}.

[20] N.J. Higham, Accuracy and stability of numerical algorithms. SIAM, 2002.

[21] M.G. Hinchey, E.I. Vassev, Method of improving system performance and survivability through through self-sacrifice, US Patent 8 (2012), 275,724.

[22] M. Hosea, L. Shampine, Analysis and implementation of tr-bdf2, Appl. Numer. Math. 20 (1996) 21–37.

[23] S. Jester, H. Falcke, Science with a lunar low-frequency array: from the dark ages of the universe to nearby exoplanets, N. Astron. Rev. 53 (2009) 1–26. https://doi.org/10.1016/j.newar.2009.02.001.

[24] M. Kaiser, W. Adams, Stereo mission overview, in: 2007 IEEE Aerospace Conference, IEEE, 2007, pp. 1–8.

[25] M. Klein-Wolt, Dark ages explorer, dex, a white paper for a low frequency radio interferometer mission to explore the cosmological dark ages for the l2, L3 ESA Cosmic Vision Program, 2013.

[26] J.J. Lissauer, I. De Pater, Fundamental Planetary Science: Physics, Chemistry and Habitability, Cambridge University Press, 2013.

[27] G.P. Liu, S. Zhang, A survey on formation control of small satellites, Proc. IEEE 106 (2018) 440–457.

[28] A.C.B. Lovell, Radio astronomical measurements from earth satellites, Proc. Roy. Soc. Lond. Math. Phys. Sci. 253 (1959) 494–500. https://doi.org/10.1098/rspa.1959.0212.

[29] D. Matson, L. Spilker, J.P. Lebreton, The cassini/huygens mission to the saturnian system, in: The Cassini-Huygens Mission, Springer, 2003, pp. 1–58.

[30] D. Oberoi, J.L. Pincon, A new design for a very low frequency spaceborne radio interferometer, Radio Sci. 40 (2005) 1–19.

[31] A. Poghosyan, I. Lluch, H. Matevosyan, A. Lamb, C. Moreno, C. Taylor, A. Golkar, J. Cote, S. Mathieu, S. Pierotti, J. Grave, J. Narkiewicz, S. Topczewski, M. Sochacki, E. Lancheros, H. Park, A. Camps, Fractionated and federated technology state of the art survey – deliverable 2.2, 2016.

[32] K. Quillien, S. Engelen, E. Gill, D. Smith, M. Arts, A.J. Boonsta, Astronomical Antenna for a Space Based Low Frequency Radio Telescope, 2013.

[33] R. Rajan, A. Boonstra, M. Bentum, M. Klein-Wolt, F. Belien, M. Arts, N. Saks, A. Van der Veen, Space-based aperture array for ultralong wavelength radio astronomy, Exp. Astron. 41 (2016) 271–306.

[34] T. Rupp, S. D'Amico, O. Montenbruck, E. Gill, Autonomous formation flying at DLR's German space operations center (GSOC), in: 58th International Astronautical Congress, Hyderabad, India, 2007.

[35] D.M. Smith, M.J. Arts, A.J. Boonstra, S.J. Wijnholds, Characterisation of astronomical antenna for space based low frequency radio telescope, in: IEEE Aerospace Conference, IEEE, 2013, pp. 1–9.

[36] T.J. Stubbs, D. Glenar, W. Farrell, R. Vondrak, M. Collier, J. Halekas, G. Delory, On the role of dust in the lunar ionosphere, Planet. Space Sci. 59 (2011) 1659–1664.

[37] V. Szebehely, Theory of Orbits: the Restricted Problem of Three Bodies, Technical Report, Yale univ, New Haven CT, 1967.

[38] A. Thompson, J. Moran, G. Swenson, Interferometry and Synthesis in Radio Astronomy, Springer Nature, 2017.

[39] url-1 NASA, State of the art of small spacecraft technology, propulsion, URL, https://www.nasa.gov/smallsat-institute/sst-soa/propulsion, 2020. (Accessed 16 July 2020).

[40] url-2 JPL, NASA, Astrodynamic constants, 2018. URL: https://ssd.jpl.nasa.gov/?constants. (Accessed 29 December 2019).

[41] B.V. Hyperion Technologies 2018 PM200. URL: https://hyperiontechnologies.nl/products/pm200/ url-3.

[42] url-4 The MathWorks Inc, Matlab, release 2019b, 2019. URL: https://nl.mathworks.com/. (Accessed 29 December 2019).

[43] url-5 The MathWorks Inc, Matlab patternsearch, URL, https://www.mathworks.com/help/gads/patternsearch.html, 2019. (Accessed 29 December 2019).

[44] url-6 [DATABASE] JPL, NASA, Horizons web-interface, Kepler space telescope ephemeris, URL, https://ssd.jpl.nasa.gov/horizons.cgi, 2018. (Accessed 29 December 2019).

[45] url-7 The MathWorks Inc, Control random number generation, URL, https://nl.mathworks.com/help/matlab/ref/rng. html, 2019. (Accessed 29 December 2019).

[46] K. Weiler, The Promise of Long Wavelength Radio Astronomy, vol. 119, Washington DC American Geophysical Union Geophysical Monograph Series, 2000, pp. 243–255.

[47] K. Weiler, B. Dennison, K. Johnston, R. Simon, W. Erickson, M. Kaiser, H. Cane, M. Desch, L. Hammarstrom, A Low-Frequency Radio Array for Space, 1988.

[48] J. Wertz, W. Larson, Space Mission Analysis and Design, 3nd ed., Microcosm, Inc., Torrance, CA (US), 1999.